Inorganic Chemistry
Article
pubs.acs.org/IC

Identification of the Vibrational Modes in the Far-Infrared Spectra of Ruthenium Carbonyl Clusters and the Effect of Gold Substitution

Trystan Bennett,[†] Rohul H. Adnan,[‡,§] Jason F. Alvino,[†] Vladimir Golovko,*[,‡] Gunther G. Andersson,*[,∥] and Gregory F. Metha*[,†]

[†]Department of Chemistry, University of Adelaide, North Terrace, Adelaide, South Australia 5005, Australia

[‡]The MacDiarmid Institute for Advanced Materials and Nanotechnology, Department of Chemistry, University of Canterbury, Christchurch 8140, New Zealand

[§]Chemistry Department, University of Malaya, 50603 Kuala Lumpur, Malaysia

[∥]Flinders Centre for NanoScale Science and Technology, Flinders University, Adelaide, South Australia 5001, Australia

S *Supporting Information*

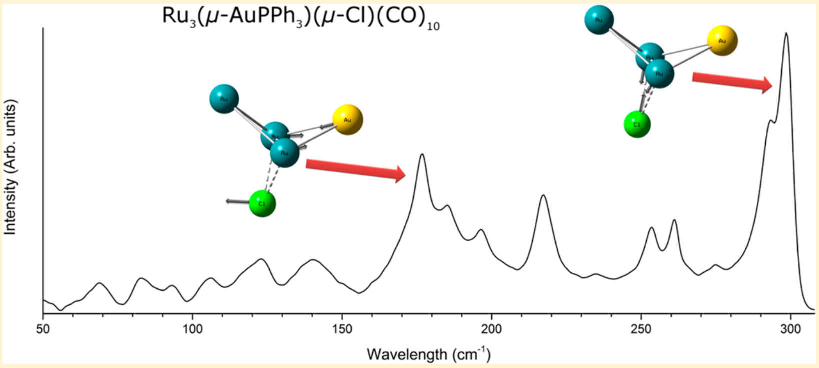

ABSTRACT: High-quality far-IR absorption spectra for a series of ligated atomically precise clusters containing Ru_3, Ru_4, and $AuRu_3$ metal cores have been observed using synchrotron radiation, the latter two for the first time. The experimental spectra are compared with predicted IR spectra obtained following complete geometric optimization of the full cluster, including all ligands, using DFT. We find strong correlations between the experimental and predicted transitions for the low-frequency, low-intensity metal core vibrations as well as the higher frequency and intensity metal−ligand vibrations. The metal core vibrational bands appear at 150 cm^{-1} for $Ru_3(CO)_{12}$, and 153 and 170 cm^{-1} for $H_4Ru_4(CO)_{12}$, while for the bimetallic $Ru_3(\mu\text{-}AuPPh_3)(\mu\text{-}Cl)(CO)_{10}$ cluster these are shifted to 177 and 299 cm^{-1} as a result of significant restructuring of the metal core and changes in chemical composition. The computationally predicted IR spectra also reveal the expected atomic motions giving rise to the intense peaks of metal−ligand vibrations at *ca.* 590 cm^{-1} for Ru_3, 580 cm^{-1} for Ru_4, and 560 cm^{-1} for $AuRu_3$. The obtained correlations allow an unambiguous identification of the key vibrational modes in the experimental far-IR spectra of these clusters for the first time.

■ INTRODUCTION

The use of chemically synthesized, atomically precise clusters as precursors in catalysis fabrication offers a unique opportunity to control the active site of the catalyst with atomic precision, enabling investigation of the correlation between chemical composition of an active site and catalytic performance. Atomically precise, chemically synthesized gold- and ruthenium-based clusters (pure and mixed-metal), such as $Au_{25}(SR)_{18}$,[1] $Ru_3(CO)_{12}$,[2] and $[PtRu_5(CO)_{15}(\mu\text{-}SnPh_2)(\mu_6\text{-}C)]$,[3] have been used as precursors in producing superior catalysts incorporating these metals over the past decade. These catalysts have been demonstrated for wide-ranging, industrially important reactions such as the processing of petroleum feedstocks,[4] selective hydrogenation yielding highly valued chemicals under mild conditions in one step,[3] the oxygen-reduction half-cell of direct methanol fuel cells,[5] and the water−gas shift reaction.[2] There has been considerable attention to the investigation of gold- and ruthenium-based ligand-stabilized metal clusters via IR, Raman, and computational approaches over the last five decades. Fewer studies, however, investigate the far-IR region of the electromagnetic spectrum, and obviously absent are studies which attempt to attribute features from IR and Raman studies to specific molecular vibrations in this region. Yet, valuable information concerning metal core vibrations can only be obtained by detailed studies of far-IR spectra. Moreover, a systematic study of series of related clusters, differing by only one metal atom per cluster core, can

Received: December 10, 2013
Published: April 23, 2014

reveal unique effects linked to the specific chemical nature of that particular metal. We hereby report the first detailed far-IR study of such a systematic series, which coupled with detailed computational modeling, enabled us to identify the shift in cluster core vibrations observed upon moving from a pure ruthenium cluster (Ru_4) to a gold-containing bimetallic cluster containing the same total number of metal atoms (i.e. Ru_3Au).

For $Ru_3(CO)_{12}$, the Raman and IR spectra below 650 cm^{-1} were first reported in 1968 by Quicksall and Spiro,[6] leading to the publication of numerous influential papers over the following two decades by authors such as Kettle and Stanghellini,[7] Battiston et al.,[8,9] Butler et al.,[10,11] Adams and Taylor,[12] and Gilson.[13,14] These authors attempted to qualitatively attribute features within the spectra to specific symmetric transitions, but no attempt was made to quantify the contribution of the metal core versus the ligands to each feature. Two publications by Lombardi and co-workers have also investigated small unligated Ru_x ($x = 2, 3$) clusters in argon matrices.[15,16] A spate of computational studies have appeared within the past decade that revisit the $Ru_3(CO)_{12}$ molecule, with Marabello and co-workers,[17,18] Schaefer and co-workers,[19,20] and Farrugia and Senn[21] all reporting calculations utilizing density functional theory (DFT) at varying theory levels. The former of these, Marabello and co-workers, have also presented experimental data which shows charge distributions throughout the $Ru_3(CO)_{12}$ molecule.[17]

For $H_4Ru_4(CO)_{12}$, while the IR absorption spectrum between 2200 and 1200 cm^{-1} has been reported several times,[22−25] we are not aware of any literature reporting IR spectra below 650 cm^{-1} apart from the Raman spectra reported by Kaesz et al.[25,26] Finally, for $Ru_3(\mu\text{-}AuPPh_3)(\mu\text{-}Cl)(CO)_{10}$, both the far-IR and the Raman spectra are absent from the literature.

In the present work we extend our previous far-IR and computational studies of gold-based clusters[27] onto ruthenium-based clusters, $Ru_3(CO)_{12}$, $H_4Ru_4(CO)_{12}$, and $Ru_3(\mu\text{-}AuPPh_3)(\mu\text{-}Cl)(CO)_{10}$ focused on the wavelength range 50−650 cm^{-1}. We apply DFT-based computational studies to aid in interpreting these spectra, and attribute individual transitions to the spectral features observed.

■ EXPERIMENTAL AND COMPUTATIONAL PROCEDURES

The $Ru_3(CO)_{12}$ cluster (CSD[28] Refcode FOKNEY, hereafter referred to as Ru_3) was prepared according to the procedure reported by Faure et al.[29] The $H_4Ru_4(CO)_{12}$ cluster (CSD Refcode FOKPAW, hereafter referred to as Ru_4) was synthesized following protocol described by Piacenti et al.[24] The $Ru_3(\mu\text{-}AuPPh_3)(\mu\text{-}Cl)(CO)_{10}$ cluster (CSD Refcode CEYTIJ, hereafter referred to as $AuRu_3$) was prepared following the method described by Lavigne et al.[30] Samples were prepared by pressing varying amounts of cluster into polyethylene (PE) to form a pellet of 7 mm diameter. Due to the wide range of absorptivity the clusters exhibited across the measurement window, the spectra were recorded at several dilutions by mass in PE. For Ru_3, the spectra reported were recorded at 1:1 Ru_3/PE (Figure 2a) and 1:5 mass dilutions (Figure 2b). For Ru_4, the spectra reported were recorded at a 1:1 Ru_4/PE mass dilution (Figure 3a, and dotted line in Figure 3b) and a 1:10 mass dilution (Figure 3b). For $AuRu_3$, the spectra reported were recorded at a 2:1 $AuRu_3$/PE mass dilution (Figure 4a) and a 1:5 mass dilution (Figure 4b).

The far-IR absorption spectra were recorded using the IFS125 Bruker FT spectrometer located at the far-IR beamline, at the Australian Synchrotron. The transmission spectrum for each sample was recorded from 50 to 650 cm^{-1}, at 1 cm^{-1} resolution utilizing the synchrotron light source (200 mA in top-up mode), with a 6 μm thick multilayer Mylar beamsplitter in combination with a Si bolometer detector. This bolometer was equipped with a 800 cm^{-1} far-IR cut-on cold-filter consisting of a 13 μm PE film overlaid with a 6 μm diamond scatter layer. All spectra were recorded at room temperature, and have been baseline corrected.

Geometry optimization and harmonic vibrational frequency calculations (including force constants, k) of the Ru_3, Ru_4, and $AuRu_3$ cluster compounds, including all ligands, were undertaken using the M06 density functional,[31] with all atoms treated using the LanL2DZ basis set and related Effective Core Potentials (ECP)[32−35] in the Gaussian 09 suite of programs.[36] This level of theory has been utilized for similar ligated metal cluster systems previously, and has been shown to give good agreement to experimental results.[27] Starting geometries were taken from X-ray crystal structures of the synthesized clusters (reported earlier by others) deposited in the Cambridge Crystallographic Database.[28] All calculations were performed as closed-shell species. The optimizations were performed in the D_{3h} and D_3, S_4, and C_1 point groups, for Ru_3, Ru_4, and $AuRu_3$, respectively. The calculations were carried out using an unpruned (199 974) grid for numerical integral evaluation, as well as tighter optimization cutoff thresholds (Gaussian keyword opt=verytight), with all other cut-offs being left at the default. Each geometry optimization was followed by a harmonic frequency calculation to confirm that the geometry was a true minimum with no imaginary frequencies. The exception to this was the D_{3h} Ru_3 structure, which optimized to a stationary point with one low-magnitude imaginary frequency (*vida infra*). To obtain the predicted IR and Raman spectra, each predicted stick spectra was convoluted with a Gaussian line shape function with 8 cm^{-1} full width at half-maximum using the GaussView 5 program, to best match the experimental spectra. Full geometric information for each optimized structure is provided in the accompanying Supporting Information.

Population analysis calculations were undertaken on the three clusters again using the Gaussian 09 suite of programs.[36] These were undertaken at the same level of theory as the optimization and frequency calculations: M06/LanL2DZ,[31−35] with an unpruned (199 974) numerical integration grid. The calculations were performed using the Gaussian keywords relevant to each population analysis method: “Pop=NBO” for natural bond order calculations,[37] “Pop=Hirshfeld” for Hirshfeld calculations,[38] “Pop=HLYGat” for the Hu−Lu−Yang model utilizing Gaussian’s standard atomic densities,[39] and “iop(6/80=1)” for the Löwdin population method,[40] while Mulliken was taken as default.[41]

■ RESULTS AND DISCUSSION

The optimized structures for the fully ligated cluster compounds discussed here are shown in the Supporting Information, Figure S1. The optimized structures for the metal cores of the Ru_3, Ru_4, and $AuRu_3$ clusters are shown in Figure 1, superimposed on the corresponding experimentally obtained crystal structures. The similarities between the structures illustrate the very close match between calculated “gas-phase” and experimental condensed phase geometries, although there

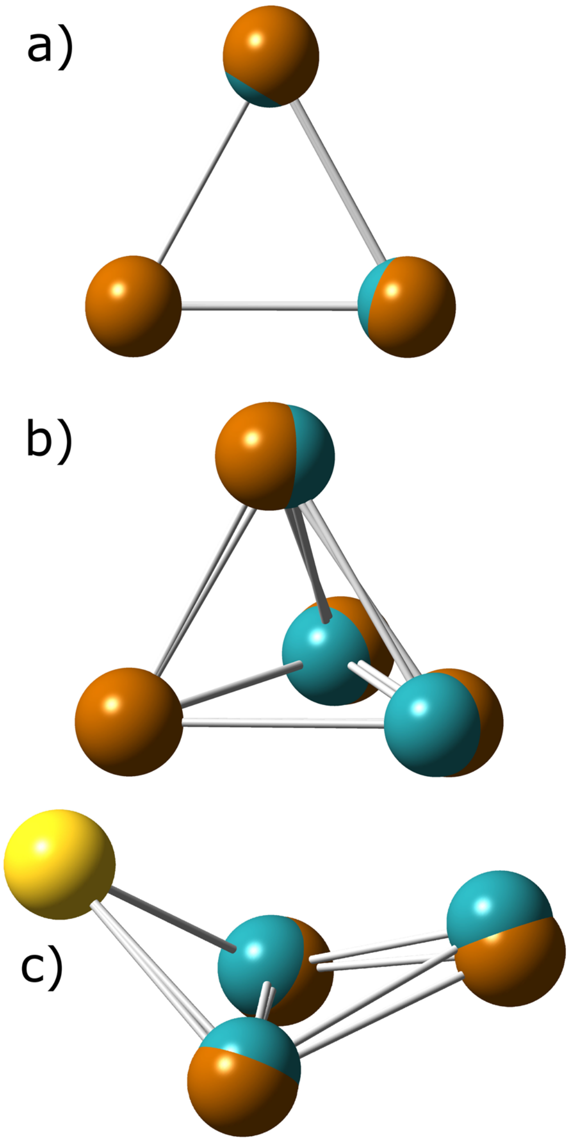

Figure 1. X-ray crystal structures (blue) and DFT optimized structures (brown) for the metal cores of the (a) Ru_3, (b) Ru_4, and (c) $AuRu_3$ clusters. The gold atom in part c is represented in yellow.

is a trend toward longer bond lengths at the optimized gas-phase energy minima. For Ru_3, this is illustrated by an elongation of the Ru−Ru bond from 2.85 to 2.90 Å. In $AuRu_3$ an elongation of the Au−Ru bond occurs from 2.75 to 2.82 Å, and an opening of the $AuRu_3$ butterfly motif from 117.2° to 123.4°. For Ru_4, however, the average Ru−Ru bond length decreased from 2.95 to 2.91 Å, most likely a result of the bridging H ligands moving further away from the center of mass.

The predicted spectra over the range 50−650 cm^{-1} for the Ru_3, Ru_4, and $AuRu_3$ clusters are shown in Figures 2−4 as dashed lines. Note that these spectra only include the calculated fundamental vibrations and do not include overtones or combination bands. For each cluster, the 50−350 cm^{-1} region (Figures 2a, 3a, and 4a) has been scaled from the calculated numbers by the functional-independent correction factor (eq 1) reported by Fielicke and co-workers for low-frequency vibrations predicted by DFT calculations, which they found afforded better agreement for far-IR transitions than traditional vibrational frequency correction schemes.[42]

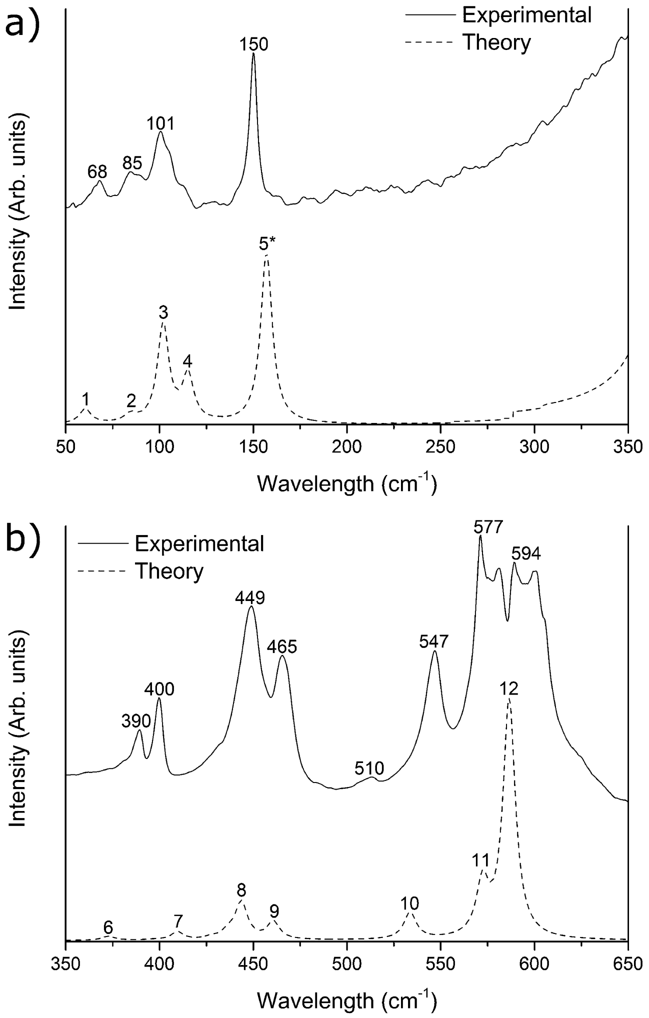

Figure 2. Experimental (solid line) and simulated (dashed line) far-IR spectrum of the Ru_3 cluster in the (a) 50−350 cm^{-1} region and (b) the 350−650 cm^{-1} region. The experimental data was recorded at (a) a 1:1 Ru_3/PE mass dilution and (b) a 1:5 mass dilution. The simulated spectrum within the 50−350 cm^{-1} region has been corrected by eq 1.

$$\tilde{\nu}_{\text{corr}} = 22\ \text{cm}^{-1} + \tilde{\nu}_{\text{calc}} \times 0.94 \qquad (1)$$

Tables 1−3 list the unscaled calculated frequency modes up to 650 cm^{-1} for each of the three clusters, with Table 1 reporting all modes with an activity greater than 0.04 km mol^{-1}, while Tables 2 and 3 list all modes that possess an IR activity greater than 0.1 km mol^{-1}. To facilitate identification of normal coordinate motions that involve significant motion of the metal core, the percentage of the total non-mass-weighted atomic motion (i.e. %Ru and %Au) is also presented within these tables. The modes are listed individually, and numbered sequentially starting at low energy. The peak numbering scheme in Tables 1−3 is the same as the one used in the simulated spectra presented in Figures 2−4. For each calculated transition, a brief description of the normal mode also appears in Tables 1−3. For each cluster, several key, core vibrations involving the metal atoms are pictorially represented in Figures 5−7, and the peaks corresponding to these transitions are highlighted within Figures 2−4, as well as Tables 1−3, with an asterisk.

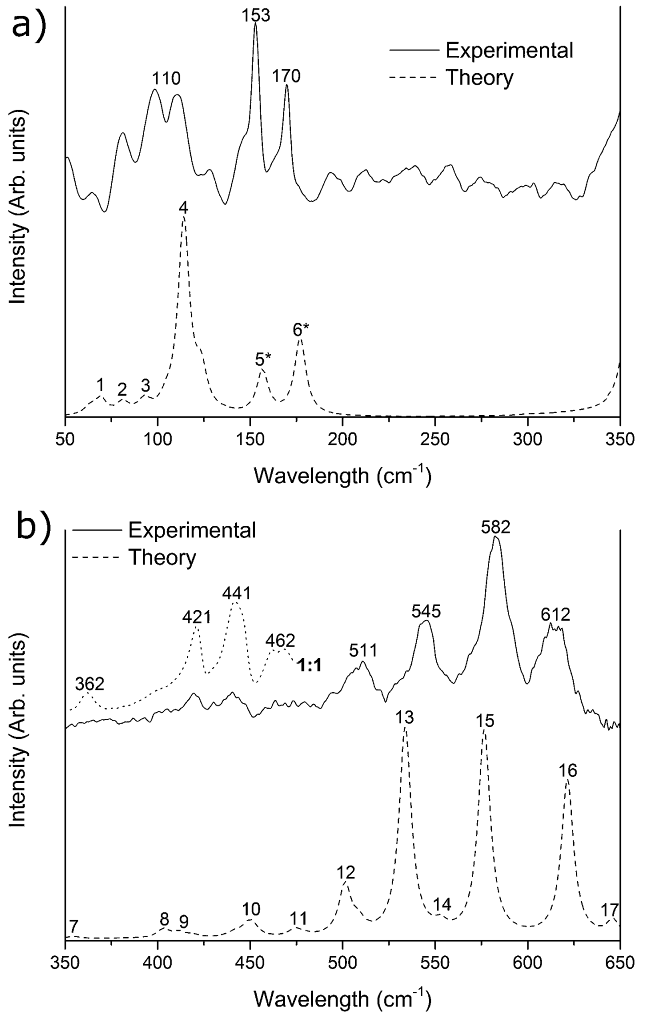

Figure 3. Experimental (solid line) and simulated (dashed line) far-IR spectrum of the Ru_4 cluster in the (a) 50−350 cm^{-1} region and (b) the 350−650 cm^{-1} region. The experimental data was recorded at (a) a 1:1 Ru_4/PE mass dilution and (b) a 1:10 mass dilution with 1:1 mass dilution (dotted line). The simulated spectrum within the 50−350 cm^{-1} region has been corrected by eq 1.

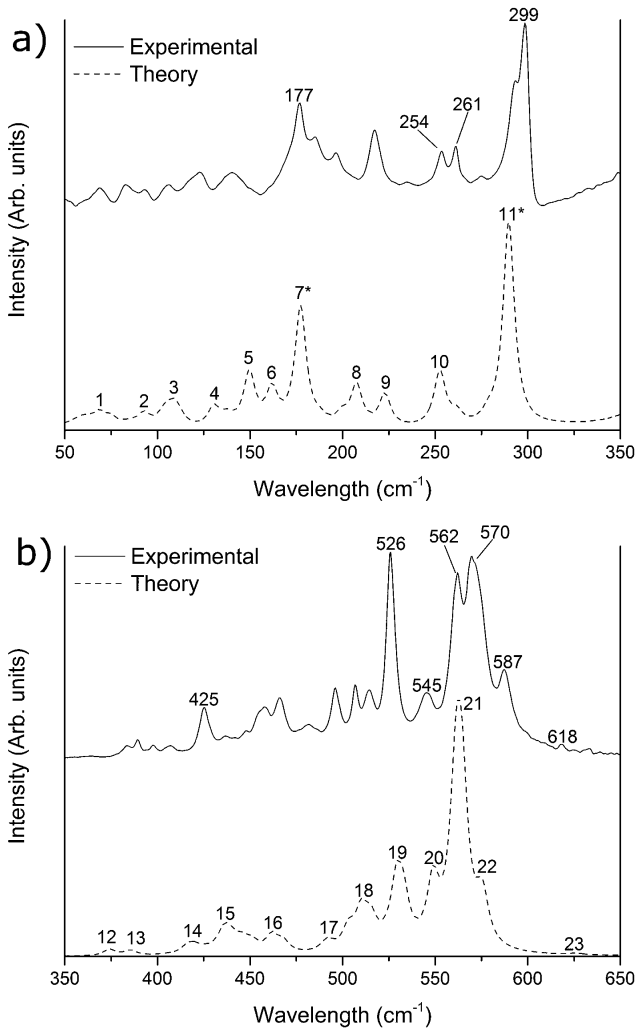

Figure 4. Experimental (solid line) and simulated (dashed line) far-IR spectrum of the $AuRu_3$ cluster in the (a) 50−350 cm^{-1} region and (b) the 350−650 cm^{-1} region. The experimental data was recorded at (a) a 2:1 $AuRu_3$/PE mass dilution and (b) a 1:5 mass dilution. The simulated spectrum within the 50−350 cm^{-1} region has been corrected by eq 1.

Also shown in Figures 2−4 are the experimental IR spectra for Ru_3, Ru_4, and $AuRu_3$ (solid lines), at varying dilutions with polyethylene (*vide supra*).

Ru_3 Cluster. Two structures were considered for the Ru_3 cluster, a D_3 structure with the Ru−(CO)$_4$ groups rotated relative to the Ru_3 plane, and a higher symmetry D_{3h} structure. The latter is identified as a transition state with a single low-magnitude imaginary frequency of 11.4*i* cm^{-1}. Visualizing this transition revealed it to correspond to a symmetric rotation of the Ru−(CO)$_4$ groups, and following this normal mode leads to the D_3 symmetry structure, as shown previously by Peng et al.[20] Our gas phase calculations predict D_3 to be the lower energy structure by *ca.* 0.1171 eV/molecule (11.299 kJ/mol), which is consistent with a computational investigation by Gervasio et al., who employed a range of basis sets and density functionals in their analysis.[18] These workers found that, without imposing symmetry constraints, the geometry optimizations would always lead to a loss of the D_{3h} symmetry, leading the authors to attribute the D_{3h} structure's stability in the solid phase to crystal packing effects. Since the D_{3h} structure has been well-established in the literature as the structure present in the solid phase,[6−8,10−14,17,18,21,43−47] it is this calculated structure that we employ for all analyses described below. A comparison between the predicted D_3 and D_{3h} far-IR spectra is available in the Supporting Information, as Figure S2.

The IR spectrum for Ru_3 in the 50−350 cm^{-1} region reveals several features (Figure 2a), the most striking of which is an intense absorption centered around 150 cm^{-1}. This feature we assign to the predicted peak 5, which is calculated to be degenerate asymmetric distortions (k = 0.33 mdyne/Å) with ca. 28% contribution from the Ru_3 core, as shown in Figure 5. At lower energy, a moderately intense broad peak observed experimentally at 101 cm^{-1} is assigned to the predicted peak 3 and the observed high-energy shoulder assigned to peak 4. We also observe two smaller intensity peaks at 68 and 85 cm^{-1}, which correspond to the low-intensity predicted absorptions 1 and 2. Adams and Taylor have previously assigned the lower energy peak to a lattice mode;[12] however, we are in agreement with Kettle and Staghellini, who argued against the need to invoke intermolecular motions to explain these peaks,[7] which is consistent with our previous work on Au-based metal clusters.[27]

Table 1. Summary of All Calculated IR-Active Vibrational Modes for the Ru_3 Cluster, Their Assignment to the Observed Far-IR Spectrum of the Cluster, and a Brief Description of the Calculated Transition Modes[a]

no.	peak (cm^{-1})	contributing vibrations[b]	IR intensity (km mol^{-1})	% Ru motion	assigned (cm^{-1})	mode description
1	41	40.8†	0.08	3.9%	68	equatorial C−Ru−C bending
2	67	66.6†	0.04	4.0%	85	equatorial C−Ru−C bending
3	85	85.0	1.0	14.4%	101	equatorial CO vertical wag
4	99	99.1†	0.2	17.7%		axial CO horizontal wag
5	144	*143.6†	0.9	28.3%	150	Ru_3 asymmetric distortion
6	373	372.6†	5.7	2.3%	390	equatorial C−Ru−C bend
7	410	396.7	1.6	7.8%	400	equatorial C−Ru−C bend
		409.5†	11.4	4.5%		equatorial C−Ru−C bend
8	444	427.3†	3.1	8.2%	449	equatorial Ru−(CO) stretches
		436.4†	9.0	12.3%		equatorial C−Ru−C asymmetric stretch
		443.6	104.7	19.6%		axial Ru−(CO) stretches
9	461	460.7†	24.6	10.8%	465	equatorial C−Ru−C symmetric stretch
10	534	533.7	74.2	3.6%	547	axial C−Ru−C bend
11	573	572.3†	73.7	13.5%	577	axial C−Ru−C bend
12	586	586.5†	332.4	12.3%	594	$Ru-(CO)_4$ bend

[a] All reported calculated vibrational frequencies are uncorrected. [b] The dagger symbol (†) denotes degenerate transition. Transitions marked with an asterisk (*) indicate large Ru_3 core contribution vibrations.

Table 2. Summary of All Calculated IR-Active Vibrational Modes for the Ru_4 Cluster, Their Assignment to the Observed Far-IR Spectrum of the Cluster, and a Brief Description of the Calculated Transition Modes[a]

no.	peak (cm^{-1})	contributing vibrations[b]	IR intensity (km mol^{-1})	% Ru motion	assigned (cm^{-1})	mode description
1	50	50.3	0.3	7.6%		$Ru-(CO)_3$ distortion
2	63	62.6†	0.1	13.0%		$Ru-(CO)_3$ distortion
3	75	75.1†	0.1	9.9%		$Ru-(CO)_3$ distortion
4	98	98.0†	2.0	20.8%	110	Ru_4 distortion
		108.1†	0.4	15.7%		(OC)−Ru−(CO) bending
5	143	*143.3†	0.5	33.7%	153	Ru_4 asymmetric distortion
6	165	*165.0	1.6	38.3%	170	Ru_4 asymmetric distortion
7	354	354.4†	1.5	3.8%	362	H_2 motion
8	403	403.1†	6.3	10.0%	421	C−Ru−C asymmetric stretch
9	411	411.6†	3.9	10.0%		Ru−C stretch
		419.0	3.6	15.6%		Ru−C stretch
10	449	438.4†	0.8	9.0%	441	$Ru-C_3$ distortion
		442.3†	6.0	6.3%		Ru−C−O bending
		451.6†	6.1	12.9%		Ru−C stretch
11	473	474.3†	5.0	12.2%	462	Ru−C stretch
		479.5	2.6	11.8%		$Ru-C_3$ bending
12	500	501.2†	35.7	12.5%	511	C−Ru−C asymmetric stretch
		508.7	15.8	16.7%		C−Ru−C asymmetric stretch
13	533	533.8†	147.6	11.7%	545	$Ru-C_3$ bending
14	553	552.8	12.0	6.3%		H_4 symmetric in plane motion
15	576	576.5	199.0	14.5%	582	C−Ru−C bending
		576.6†	46.2	12.6%		C−Ru−C bending
16	621	621.5†	111.0	10.5%	612	H_2 motion
17	646	646.0	22.0	8.7%		H_4 motion

[a] All reported calculated vibrational frequencies are uncorrected. [b] The dagger symbol (†) denotes degenerate transition. Transitions marked with an asterisk (*) indicate large Ru_4 core contribution vibrations.

The IR spectrum for Ru_3 within the 350−650 cm^{-1} region shows five main features (Figure 2b), with the main absorbance feature within this region being a large, broad doublet at 577 and 594 cm^{-1}. We assign this doublet to the predicted intense peaks 11 and 12, transitions resulting from axial C−Ru−C bending motions, and $Ru-(CO)_4$ group bending motions, respectively. The shoulder on the high energy side of the 594 cm^{-1} peak is consistent with that observed in the literature.[7,12] Below this, a moderately intense absorption at 547 cm^{-1} is assigned to peak 10, which is predicted to originate from a single transition corresponding to a C−Ru−C bending motion. The weak, broad peak observed at 510 cm^{-1} is not found within the predicted spectra.

The two remaining features within this region are both doublets, with the higher intensity 449 and 465 cm^{-1} pair closely matching predicted peaks 8 and 9 in both position and relative intensity. These peaks are attributed to a single intense $(CO)_{ax}-Ru$ stretching transition at 444 cm^{-1}, and a pair of degenerate $(CO)_{eq}-Ru$ group stretches, respectively. The lower intensity pair of peaks observed at 390 and 400 cm^{-1}

Table 3. Summary of all Calculated IR-Active Vibrational Modes for the $AuRu_3$ Cluster, Their Assignment to the Observed Far-IR Spectrum of the Cluster, and a Brief Description of the Calculated Transition Modes[a]

no.	peak (cm^{-1})	contributing vibrations	IR intensity (km mol^{-1})	% Au motion	% Ru motion	% P motion	% Cl motion	assigned (cm^{-1})	mode description
1	50	51.8	0.1	1.8%	3.7%	0.3%	0.5%		P−Ph motion
		56.4	0.3	0.6%	5.8%	0.7%	2.1%		(OC)−Ru−(CO) bending
		63.3	0.1	2.1%	3.8%	0.6%	0.7%		P−Ph motion
2	75	75.0	0.4	4.3%	8.9%	3.5%	2.6%		Ru_3−Au distortion
		76.5	0.1	2.1%	7.7%	1.2%	2.8%		(OC)−Ru−(CO) bending
3	92	86.4	0.3	8.4%	7.2%	1.4%	2.7%		Ru_2−Au distortion
		87.7	0.1	2.8%	5.0%	1.7%	3.5%		C−Ru−C bending
		89.1	0.2	4.8%	6.8%	2.4%	3.0%		C−Ru−C bending
		92.2	0.7	1.2%	14.9%	2.3%	5.9%		Ru−Cl−Ru stretching
		95.1	0.3	2.1%	15.0%	2.0%	1.4%		Ru_3 distortion
4	116	115.3	0.8	3.2%	17.5%	2.2%	4.3%		Ru_3−Cl distortion
		120.5	0.1	2.4%	7.0%	2.9%	1.1%		(OC)−Ru−(CO) bending
		123.6	0.3	6.7%	24.8%	2.0%	1.2%		Ru_3−Au distortion
5	136	135.8	2.2	3.2%	13.2%	1.7%	3.1%		Ru_3−Au distortion
6	149	148.5	1.1	4.9%	14.4%	1.2%	9.9%		Cl motion
		149.5	0.4	3.3%	22.1%	1.5%	6.7%		Ru_3−Au distortion
7	165	*165.2	5.0	8.6%	15.3%	0.0%	7.3%	177	Cl−Ru_3−Au distortion
		176.4	0.2	3.1%	26.7%	1.7%	5.8%		Ru_3 symmetrical distortion
8	197	189.2	0.5	2.1%	1.4%	0.4%	0.4%		P−C−C bending
		197.4	1.7	1.1%	0.0%	0.3%	0.5%		Ph group rocking
9	214	213.7	1.4	1.1%	0.0%	2.0%	0.0%		Ph group rocking
10	245	243.4	0.2	0.8%	23.3%	1.3%	31.2%	254 and 261	Ru_2−Cl asymmetric motion
		245.4	2.1	0.0%	0.0%	1.7%	0.0%		Ph_3−P bending
		254.8	0.5	0.0%	0.0%	1.0%	0.5%		Ph_3−P bending
11	285	273.0	0.4	0.0%	0.0%	0.7%	0.0%	299	Ph_3−P bending
		*284.8	8.6	0.0%	21.4%	3.4%	37.1%		Ru_2Cl stretching
12	374	371.6	0.2	0.0%	0.8%	1.9%	0.5%		Ru−C−O bending
		373.9	6.3	0.0%	3.8%	1.1%	1.0%		C−Ru−C bending
		374.8	2.7	0.0%	4.2%	1.1%	1.4%		Ru−C−O bending
13	385	385.4	6.0	0.0%	4.8%	0.2%	0.0%		Ru−C−O bending
		386.0	1.3	0.0%	3.2%	2.2%	0.0%		Ru−C−O bending
		399.8	0.2	0.0%	11.5%	1.8%	0.0%		Ru−C stretching
14	419	404.8	0.7	0.0%	2.1%	0.0%	0.0%		Ph group out-of-plane distortion
		408.4	0.1	0.0%	0.0%	1.0%	0.0%		Ph group out-of-plane distortion
		415.2	5.6	0.0%	10.4%	1.1%	0.6%		C−Ru−C asymmetric stretching
		417.4	6.2	0.0%	9.2%	1.1%	1.4%		C−Ru−C asymmetric stretching
		420.2	8.2	0.0%	10.8%	0.0%	2.0%		Ru−C−O bending
15	437	425.0	3.5	0.0%	5.4%	0.0%	1.2%	425	C−Ru−C bending
		428.5	1.8	0.0%	7.5%	0.0%	0.6%		Ru−C−O bending
		432.0	2.8	0.8%	2.0%	0.0%	0.0%		Ph group out-of-plane distortion
		435.4	3.3	0.7%	2.9%	0.4%	0.3%		Ph group out-of-plane distortion
		436.1	25.7	0.0%	11.9%	0.4%	0.5%		Ru−(CO) stretching
		439.0	4.2	0.7%	5.0%	0.6%	0.3%		Ru−C_3 bending
		439.8	11.8	0.7%	5.9%	0.9%	0.3%		Ru−C_3 bending
		443.4	6.3	0.0%	10.1%	0.7%	0.4%		Ru−(CO) stretching
		446.4	12.0	0.0%	8.5%	0.6%	0.7%		C−Ru−C bending
		450.5	8.3	0.0%	9.1%	0.9%	0.4%		CO−Ru stretching
		452.5	5.4	0.0%	0.9%	1.1%	0.0%		PPh_3 distortion
16	462	461.8	24.3	0.0%	10.8%	1.4%	0.9%		Ru−C_3 bending
		468.0	15.0	0.0%	12.1%	1.0%	1.3%		Ru−C_3 bending
17	492	489.3	1.5	0.0%	4.7%	1.8%	0.0%		Ru−C_4 bending
		491.9	14.5	0.0%	6.4%	10.6%	0.4%		Ru−C_2 bending
18	511	503.2	29.4	0.0%	0.8%	8.3%	0.0%		Ph group out-of-plane distortion
		510.1	50.6	0.0%	11.5%	1.7%	0.4%		C−Ru−C bending

Table 3. continued

no.	peak (cm^{-1})	contributing vibrations	IR intensity ($km\ mol^{-1}$)	% Au motion	% Ru motion	% P motion	% Cl motion	assigned (cm^{-1})	mode description
		515.3	34.8	0.0%	3.5%	4.7%	0.0%		Ph_3−P distortion
		517.7	1.8	0.0%	10.8%	2.5%	0.5%		Ru−C_4 bending
19	530	523.3	3.7	0.0%	15.2%	2.2%	0.4%	526	Ru−C_3 bending
		529.2	84.5	1.0%	0.8%	1.8%	0.0%		Ph group out-of-plane distortion
		532.8	57.7	0.0%	13.0%	2.2%	0.0%		C−Ru−C bending
20	549	548.9	87.5	0.0%	11.0%	10.6%	0.6%	545	C−Ru−C_2 bending
21	563	561.3	207.9	0.0%	13.7%	1.0%	0.4%	562 and 570	C−Ru−C bending
		564.4	193.0	0.0%	13.8%	0.6%	0.4%		C−Ru−C bending
22	574	575.0	37.5	0.0%	12.4%	0.0%	0.4%	587	Ru−C_3 bending
		576.0	32.2	0.0%	11.9%	0.3%	0.0%		Ru−C_3 bending
23	626	625.0	0.3	0.0%	0.0%	8.2%	0.0%	618	Ph group in-plane distortion
		626.4	1.7	0.0%	0.0%	7.1%	0.0%		Ph group in-plane distortion

[a] All reported calculated vibrational frequencies are uncorrected. Transitions marked with an asterisk (*) indicate large core metal contribution vibrations.

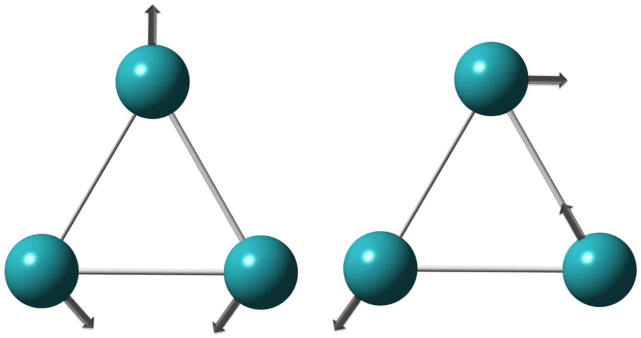

Figure 5. Calculated normal mode displacements associated with the degenerate *e*′ cluster core vibrations for Ru_3 at 143.6 cm^{-1}. Note that ligands are omitted for clarity.

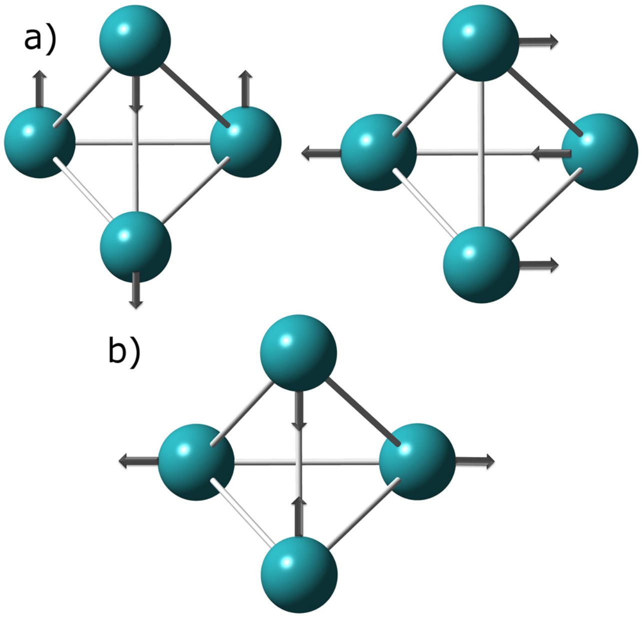

Figure 6. Calculated normal mode displacements associated with the cluster core vibrations for Ru_4 at (a) degenerate modes at 143.3 cm^{-1} and (b) 165.0 cm^{-1}. Note that ligands are omitted for clarity.

are attributed to the relatively weaker predicted pair of features labeled 6 and 7, which are due to $(CO)_{eq}$−Ru bending motions.

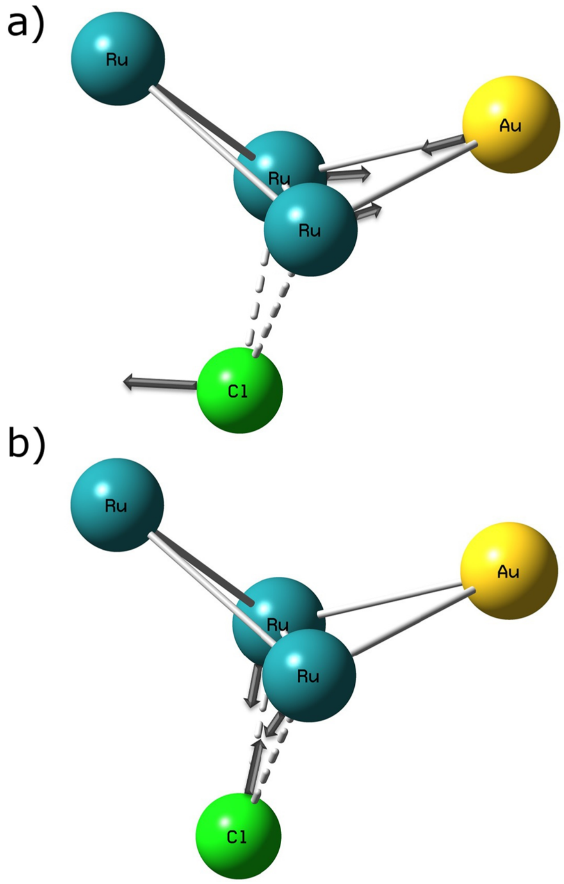

Figure 7. Calculated normal mode displacements associated with the cluster core vibrations for $AuRu_3$ at (a) 165.2 cm^{-1} and (b) 284.8 cm^{-1}. Note that ligands are omitted for clarity.

The predicted Ru_3 Raman spectrum is shown in the Supporting Information, as Figure S3a. The low-frequency (sub-650 cm^{-1}) experimental Raman spectrum has been reported several times before in the literature, at ambient conditions,[6,7,10,11] 100 K,[12] and 15 K,[11] and also at a range of pressures up to 15.8 GPa.[45] There is general agreement between our predicted spectra (Supporting Information Figure S3a), and the spectra published by Kettle and Staghellini,[7] with particular reference to the main, key feature around 450 cm^{-1}, which matches in both shape and relative intensity; this peak is due to a highly symmetric Ru−(CO) stretching mode.

The Raman spectrum of the bare metal cluster, Ru_3, has also been reported by Lombardi and co-workers, which was taken by depositing the cluster into an argon matrix.[15] They observed the symmetric stretch of Ru_3 to occur at 303.6 cm^{-1}, and calculated a force constant of 1.86 mdyne/Å. Within our predicted spectra, we find a shifting of this symmetric stretch to 177 cm^{-1} (k = 0.65 mdyne/Å), which appears as an intense peak centered around 180 cm^{-1} (Supporting Information Figure S3a). This shift is consistent with the removal of electron density from the metal core by the ligands, as observed in the reduced force constant of the vibration.

Ru_4 Cluster. The IR spectrum of Ru_4 has been previously reported in the 2200−1200 cm^{-1} region several times;[22−25] however, no reports exist at lower frequency.

The experimental spectrum of Ru_4 between 50 and 350 cm^{-1} (Figure 3a) reveals a "multiplet" centered around 110 cm^{-1}, and two sharp peaks at 153 and 170 cm^{-1}. The latter two peaks are assigned to peaks 5 (k = 0.35 mdyne/Å) and 6 (k = 0.53 mdyne/Å) which are predicted to contain 34% and 38% ruthenium cluster core contribution, respectively, as schematically represented in Figure 6a (degenerate) and Figure 6b. The predicted force constants of these vibrations are consistent with the calculation for Ru_3, with the lower energy vibration being almost identical in energy, with very similar k (cf. 0.33 mdyne/Å for the Ru_3 transition at 150 cm^{-1}). The higher energy vibration has a similar reduced mass but is shifted due to its higher k. The multiplet feature is assigned to predicted peak 4, which is due to Ru_4 core distortions as well as Ru−(CO) bending motions. The rounded multiplet nature of this experimental peak, as opposed to the sharp singlet nature of the two higher energy features, is attributed to distortions from the low-frequency oscillations in the data within this region, which are due to fringing effects.

The experimental spectrum between 350 and 480 cm^{-1} (Figure 3b) exhibits four features, which closely match the predicted spectra within this region. The lowest energy feature at 362 cm^{-1} is assigned to peak 7, which is a weak, broad feature with two underlying transitions, both due to motion of the hydrogen ligands. The shouldered peak at 421 cm^{-1} is assigned to peaks 8 and 9, which are predicted to be due to Ru−C stretch modes. The broad intense feature at 441 cm^{-1} is assigned to the predicted peak around 450 cm^{-1} (peak 10), which is a collection of several transitions, composed primarily of degenerate Ru−C stretches and Ru−C−O bending motions. The highest energy feature in this region is a broad doublet at 462 cm^{-1}, which is assigned to peak 11, which is due to three transitions composed of Ru−C stretches, and a $Ru-C_3$ group bending motion.

The higher energy region, 480−650 cm^{-1}, contains four peaks of significantly higher intensity than the rest of the spectrum. The first three peaks, at 511, 545, and 582 cm^{-1}, are assigned to three corresponding predicted high intensity features 12, 13, and 15, which are all due to Ru−C bending and stretching motions. The final peak at 612 cm^{-1} is assigned to peak 16, an intense peak due to hydrogen ligand motions.

The predicted Raman spectrum for Ru_4 is shown in Figure S3b (Supporting Information). The Raman spectrum between 350 and 650 cm^{-1} has been previously reported by Kaesz et al.[25,26] This reported spectrum largely matches our predicted spectrum, with the fingerprint peak of a very strong absorption at 472 cm^{-1} matching the predicted large very intense feature (Supporting Information Figure S3b) at 473 cm^{-1}, which arises from a highly symmetric Ru−(CO) stretching motion.

For Ru_4, the symmetric stretch of the metal core is predicted to occur at 187 cm^{-1} (k = 0.71 mdyne/Å), with a reduced mass of 34.1 amu. The Ru_3 counterpart, which has the symmetric stretch predicted to occur at 177 cm^{-1} (k = 0.65 mdyne/Å), has a reduced mass of 35.5 amu. The calculated increase in k and smaller reduced mass as the cluster gains a fourth Ru atom leads to the predicted shift to higher wavenumbers for this motion.

$AuRu_3$ Cluster. The experimental IR spectrum for $AuRu_3$ between 50 and 250 cm^{-1} (Figure 4a) consists of three large singlets, at 177, 218, and 299 cm^{-1}, and a doublet at 254 and 261 cm^{-1}. There are also many lower intensity peaks within the spectrum, including a multiplet below 170 cm^{-1}, and several shoulders on both the 177 and 299 cm^{-1} peaks. The peaks at 177 and 299 cm^{-1} closely match two intense transitions: peak 7 predicted at 165 (k = 0.37 mdyne/Å) and peak 11 at 285 cm^{-1} (k = 1.65 mdyne/Å). These peaks are attributed to normal modes with large metal core distortions; the former a $AuRu_3Cl$ core distortion (9% Au, 15% Ru contribution), and the latter a Ru_2Cl stretching motion (21% Ru contribution). These two transitions are illustrated in Figure 7.

The force constants of these two transitions are predicted to be consistent with those predicted for both the Ru_3 and Ru_4 molecule. The peak observed at 177 cm^{-1} for $AuRu_3$ is predicted to possess a slightly higher k than either the 150 cm^{-1} feature of Ru_3, or the 153 cm^{-1} feature of Ru_4 (0.37 mdyne/Å, cf. 0.33 and 0.35 for Ru_3 and Ru_4, respectively), and also has a smaller reduced mass (23.2 amu, cf. 26.8 and 28.7 for Ru_3 and Ru_4, respectively), leading to its appearance at higher wavenumbers. Finally, the 299 cm^{-1} IR peak of $AuRu_3$ is predicted to have a force constant very similar to that of the unligated Ru_3 as reported by Lombardi and co-workers:[15] 1.65 mdyne/Å, compared to 1.86 for the unligated Ru_3 cluster.

The doublet at 254 and 261 cm^{-1} is ascribed to another vibration with significant metal core motion (peak 10, 23% Ru contribution). Peak 10 consists of three transitions, which may explain the doublet appearance in the spectra. The transition at 218 cm^{-1} could be assigned to either of peaks 8 and 9, both having minimal (<5%) contribution from the metal core. Below 175 cm^{-1}, the calculations predict myriad smaller transitions (peaks 1−6), which bears some resemblance to the barely discernible peaks in the experimental spectrum.

Within the 350−650 cm^{-1} region of $AuRu_3$ we predict the appearance of more than 40 separate transitions (Figure 4b). The experimental spectrum also shows a large number of smaller peaks, especially between 375 and 550 cm^{-1}. As within the lower energy range, due to the complexity of the spectrum there are few that are assignable to specific transitions. Two peaks which can be unambiguously assigned are a moderate intensity singlet at 425 cm^{-1}, and a very strong singlet centered around 526 cm^{-1}, which we assign to peaks 15 and 19, respectively. These peaks are predicted to contain contributions from multiple transitions, due primarily to a combination of Ru−(CO) stretches and bends, C−Ru−C bends, and phenyl group distortions. A final smaller peak is observed at 545 cm^{-1}, which is assigned to peak 20 at 549 cm^{-1}. This predicted peak arises from a single transition, which is due to $C-Ru-C_2$ bending.

Above 550 cm^{-1}, the key feature is a large, broad doublet, at 562 and 570 cm^{-1}, which is assigned to peak 21. This peak is predicted to be due to C−Ru−C bending motions, with the Ru contribution of 14%. A predicted high energy shoulder, peak 22, is assigned to a high energy shoulder on the large experimentally observed doublet, occurring at 587 cm^{-1}. Finally, the highest energy transition predicted within this region, peak 23, is assigned to the small peak occurring at 618 cm^{-1}.

The predicted Raman spectrum is presented in Figure S3c (Supporting Information). The experimental spectrum has never been reported previously in the literature, but we predict a large number of features, with a key high intensity peak occurring at 450 cm^{-1}, which is due to the Ru−(CO) stretching, as was the case with the intense features in both the Ru_3 and Ru_4 Raman spectra. A symmetric stretch involving the Ru_3 group and the Cl atom is predicted to occur at 176 cm^{-1} (k = 0.57 mdyne/Å, 31.3 amu). This is comparable in energy to the 177 cm^{-1} peak predicted for the Ru_3 cluster, which has both a larger force constant and reduced mass (k = 0.65 mdyne/Å, 35.5 amu).

Population Analysis Calculations. For the $Ru_3(CO)_{12}$ cluster, the atomic charge distribution was calculated by several methods: Mulliken,[41] NBO,[37] Hirshfeld,[38] Löwdin,[40] and the Hu−Lu−Yang model utilizing Gaussian's standard atomic densities.[39] These values, as well as experimentally derived data,[17] are presented in Table 4. The experimental charges show approximately the same positive charge on both the Ru and C atoms (0.61 and 0.60, respectively), with a slightly larger in magnitude negative charge residing on the oxygen atoms (−0.75). Computationally, all population analysis methods predict a negatively charged Ru_3 core, with less negatively charged O atoms, balanced with positively charged C atoms. The only exception to this is the Mulliken method, which, in accordance with the experimental data, predicts a positively charged Ru_3 core with less positive C atoms, and negatively charged O atoms. However, none of the methods match the experimental values particularly well. This may be due to either shortcomings within the population analyses utilized, or differences between the modeling (gas phase) versus experimental (crystal structure) conditions.

Table 4. Experimental and Theoretical Charge Distribution for the Atom Types in the Ru_3, Ru_4, and $AuRu_3$ Clusters

	exptl[17]	Mulliken	Hirshfeld	Löwdin	HLYGat	NBO
Ru_3						
Ru	0.61	0.31	−0.19	−0.97	−1.14	−1.33
C	0.60	0.05	0.17	0.33	0.59	0.75
O	−0.75	−0.12	−0.12	−0.09	−0.30	−0.42
Ru_4						
Ru		0.05	−0.17	−0.97	−1.58	−1.31
C		0.08	0.18	0.34	0.68	0.80
O		−0.13	−0.12	−0.09	−0.30	−0.42
H		0.11	−0.02	0.20	0.44	0.17
$AuRu_3$						
Au		−0.13	−0.15	−0.38	0.27	0.18
Ru		0.18	−0.15	−0.98	−0.79	−1.28
Cl		−0.05	−0.19	0.27	−0.21	−0.05
C (CO)		0.08	0.17	0.34	0.52	0.77
O		−0.15	−0.13	−0.10	−0.30	−0.43
P		0.60	0.36	1.05	−1.20	0.88
C (Ph)		−0.21	−0.05	−0.15	−0.08	−0.22
H		0.24	0.06	0.15	0.18	0.23

For $H_4Ru_4(CO)_{12}$, a similar trend is predicted, with all methods except Mulliken predicting a negatively charged Ru core, with positive carbon and hydrogen atoms, and negative oxygen atoms. This trend continues to $AuRu_3$, with a negatively charged metal core predicted, with an overall neutral charge on the phenyl rings, a large positive charge on the phosphorus atom, and negative oxygen atoms and positive carbon atoms in the CO ligands.

■ CONCLUSIONS

The low-frequency and low-intensity metal core vibrations for $H_4Ru_4(CO)_{12}$ and $Ru_3(\mu\text{-}AuPPh_3)(\mu\text{-}Cl)(CO)_{10}$ are reported for the first time. While for pure Ru-based clusters metal core vibrations are observed at 150 cm^{-1} for Ru_3, 153 and 170 cm^{-1} for Ru_4, substitution with Au results in a significant shift to 177 and 299 cm^{-1} for a mixed-metal $AuRu_3$ cluster, most likely due to significant change in metal core geometry (tetrahedral to butterfly) and chemical composition. More intense vibrations involving strong metal−ligand contributions occur near 590 cm^{-1} for Ru_3, 580 cm^{-1} for Ru_4, and 560 cm^{-1} for $AuRu_3$. Strong correlations between experimentally obtained (synchrotron) and computationally predicted (DFT) far-IR spectra of $Ru_3(\mu\text{-}AuPPh_3)(\mu\text{-}Cl)(CO)_{10}$, $H_4Ru_4(CO)_{12}$, and $Ru_3(CO)_{12}$ enabled explicit identification of the nature of the key transitions for each of these clusters for the first time.

■ ASSOCIATED CONTENT

Supporting Information

Figure S1 contains full images of the ligated metal clusters. Figure S2 contains simulated far-IR spectra of Ru_3 optimized to both the D_3 and D_{3h} structures in (a) the (uncorrected) region 50−350 cm^{-1} and (b) the region 350−650 cm^{-1}. Figure S3 contains simulated Raman spectra of (a) the Ru_3 cluster in the region 20−650 cm^{-1}, (b) the Ru_4 cluster in the region 20−650 cm^{-1}, and (c) the $AuRu_3$ cluster in the region 20−800 cm^{-1}. The atomic coordinates for the optimized structures of each of the three clusters are available in Tables S1−S3. This material is available free of charge via the Internet at http://pubs.acs.org.

■ AUTHOR INFORMATION

Corresponding Author

*Phone: +61 8 8303 5943 (G.F.M.). Fax: +61 8 8303 4358 (G.F.M.). E-mail: greg.metha@adelaide.edu.au (G.F.M.).

Notes

The authors declare no competing financial interest.

■ ACKNOWLEDGMENTS

This work was supported by a grant from the Australian Synchrotron (AS123/HRIR/5251). Financial support from the Centre for Energy Technologies at the University of Adelaide, the MacDiarmid Institute for Advanced Materials and Nanotechnology, the University of Canterbury, and the University of Malaya is gratefully acknowledged. Computing resources provided by the National Computational Infrastructure (NCI) Facility, and eResearch SA is also gratefully acknowledged. The authors would also like to thank Dr Dominique Appadoo for his advice recording the infrared spectra at the Australian Synchrotron, and Prof. Emer. Michael Bruce (Adelaide) for discussions regarding paramagnetism in small metal clusters.

■ REFERENCES

(1) Zhu, Y.; Qian, H.; Drake, B. A.; Jin, R. *Angew. Chem., Int. Ed.* **2010**, *49*, 1295−1298.

(2) Laine, R. M.; Rinker, R. G.; Ford, P. C. *J. Am. Chem. Soc.* **1977**, *99*, 252−253.

(3) Hungria, A. B.; Raja, R.; Adams, R. D.; Captain, B.; Thomas, J. M.; Midgley, P. A.; Golovko, V.; Johnson, B. F. G. *Angew. Chem., Int. Ed.* **2006**, *45*, 4782−4785.

(4) Los Reyes, J. A.; Göbölös, S.; Vrinat, M.; Breysse, M. *Catal. Lett.* **1990**, *5*, 17−24.

(5) Shukla, A.; Raman, R. *Annu. Rev. Mater. Res.* **2003**, *33*, 155−168.

(6) Quicksall, C. O.; Spiro, T. G. *Inorg. Chem.* **1968**, *7*, 2365−2369.

(7) Kettle, S. F. A.; Stanghellini, P. L. *Inorg. Chem.* **1979**, *18*, 2749−2754.

(8) Battiston, G. A.; Bor, G.; Dietler, U. K.; Kettle, S. F.; Rossetti, R.; Sbrignadello, G.; Stanghellini, P. L. *Inorg. Chem.* **1980**, *19*, 1961−1973.

(9) Battiston, G. A.; Sbrignadello, G.; Bor, G. *Inorg. Chem.* **1980**, *19*, 1973−1977.

(10) Butler, I. S.; Xu, Z. H.; Darensbourg, D. J.; Pala, M. *J. Raman Spectrosc.* **1987**, *18*, 357−363.

(11) Kishner, S.; Fitzpatrick, P. J.; Plowman, K. R.; Butler, I. S. *J. Mol. Struct.* **1981**, *74*, 29−37.

(12) Adams, D. M.; Taylor, I. D. *J. Chem. Soc., Faraday Trans. 2* **1982**, *78*, 1561−1571.

(13) Gilson, T. R. *J. Chem. Soc., Dalton Trans.* **1984**, 149−153.

(14) Gilson, T. R.; Evans, J. *J. Chem. Soc., Dalton Trans.* **1984**, 155−159.

(15) Fang, L.; Shen, X.; Chen, X.; Lombardi, J. R. *Chem. Phys. Lett.* **2000**, *332*, 299−302.

(16) Wang, H.; Liu, Y.; Haouari, H.; Craig, R.; Lombardi, J. R.; Lindsay, D. M. *J. Chem. Phys.* **1997**, *106*, 6534−6537.

(17) Gervasio, G.; Bianchi, R.; Marabello, D. *Chem. Phys. Lett.* **2005**, *407*, 18−22.

(18) Gervasio, G.; Marabello, D.; Bianchi, R.; Forni, A. *J. Phys. Chem. A* **2010**, *114*, 9368−9373.

(19) Feng, X.; Gu, J.; Xie, Y.; King, R. B.; Schaefer, H. F. *J. Chem. Theory Comput.* **2007**, *3*, 1580−1587.

(20) Peng, B.; Li, Q.-S.; Xie, Y.; King, R. B.; Schaefer Iii, H. F. *Dalton Trans.* **2008**, 6977−6986.

(21) Farrugia, L. J.; Senn, H. M. *J. Phys. Chem. A* **2011**, *116*, 738−746.

(22) Johnson, B.; Johnston, R.; Lewis, J.; Robinson, B.; Wilkinson, G. *J. Chem. Soc. A* **1968**, 2856−2859.

(23) Johnson, B.; Lewis, J.; Williams, I. *J. Chem. Soc. A* **1970**, 901−903.

(24) Piacenti, F.; Bianchi, M.; Frediani, P.; Benedetti, E. *Inorg. Chem.* **1971**, *10*, 2759−2763.

(25) Knox, S.; Koepke, J.; Andrews, M.; Kaesz, H. *J. Am. Chem. Soc.* **1975**, *97*, 3942−3947.

(26) Kaesz, H. D.; Saillant, R.-B. *Chem. Rev.* **1972**, *72*, 231−281.

(27) Alvino, J. F.; Bennett, T.; Anderson, D. P.; Donoeva, B.; Ovoshchnikov, D.; Adnan, R.; Appadoo, D. R.; Golovko, V.; Andersson, G. G.; Metha, G. F. *RSC Adv.* **2013**, *3*, 22140−22149.

(28) Allen, F. *Acta Crystallogr., Sect. B* **2002**, *58*, 380−388.

(29) Fauré, M.; Saccavini, C.; Lavigne, G. *Chem. Commun.* **2003**, 1578−1579.

(30) Lavigne, G.; Papageorgiou, F.; Bonnet, J. J. *Inorg. Chem.* **1984**, *23*, 609−613.

(31) Zhao, Y.; Truhlar, D. G. *Theor. Chem. Acc.* **2008**, *120*, 215−241.

(32) Dunning, T., Jr.; Hay, P. *Mod. Theor. Chem.* **1977**, *3*, 1−28.

(33) Hay, P. J.; Wadt, W. R. *J. Chem. Phys.* **1985**, *82*, 270−283.

(34) Hay, P. J.; Wadt, W. R. *J. Chem. Phys.* **1985**, *82*, 299−310.

(35) Wadt, W. R.; Hay, P. J. *J. Chem. Phys.* **1985**, *82*, 284−298.

(36) Frisch, M. J.; Trucks, G. W.; Schlegel, H. B.; Scuseria, G. E.; Robb, M. A.; Cheeseman, J. R.; Scalmani, G.; Barone, V.; Mennucci, B.; Petersson, G. A.; Nakatsuji, H.; Caricato, M.; Li, X.; Hratchian, H. P.; Izmaylov, A. F.; Bloino, J.; Zheng, G.; Sonnenberg, J. L.; Hada, M.; Ehara, M.; Toyota, K.; Fukuda, R.; Hasegawa, J.; Ishida, M.; Nakajima, T.; Honda, Y.; Kitao, O.; Nakai, H.; Vreven, T.; Montgomery, J. J. A.; Peralta, J. E.; Ogliaro, F.; Bearpark, M.; Heyd, J. J.; Brothers, E.; Kudin, K. N.; Staroverov, V. N.; Kobayashi, R.; Normand, J.; Raghavachari, K.; Rendell, A.; Burant, J. C.; Iyengar, S. S.; Tomasi, J.; Cossi, M.; Rega, N.; Millam, N. J.; Klene, M.; Knox, J. E.; Cross, J. B.; Bakken, V.; Adamo, C.; Jaramillo, J.; Gomperts, R.; Stratmann, R. E.; Yazyev, O.; Austin, A. J.; Cammi, R.; Pomelli, C.; Ochterski, J. W.; Martin, R. L.; Morokuma, K.; Zakrzewski, V. G.; Voth, G. A.; Salvador, P.; Dannenberg, J. J.; Dapprich, S.; Daniels, A. D.; Farkas, Ö.; Foresman, J. B.; Ortiz, J. V.; Cioslowski, J.; Fox, D. J. *Gaussian 09, Revision C.01*; Gaussian, Inc.: Wallingford, CT, 2009.

(37) Glendening, E. D.; Reed, A. E.; Carpenter, J. E.; Weinhold, F. *NBO Version 3.1*.

(38) Hirshfeld, F. *Theor. Chim. Acta* **1977**, *44*, 129−138.

(39) Hu, H.; Lu, Z.; Yang, W. *J. Chem. Theory Comput.* **2007**, *3*, 1004−1013.

(40) Löwdin, P.-O. On the Nonorthogonality Problem. In *Advances in Quantum Chemistry*; Per-Olov, L., Ed.; Academic Press: New York, 1970; Vol. *5*, pp 185−199.

(41) Mulliken, R. S. *J. Chem. Phys.* **1955**, *23*, 1833−1840.

(42) Lin, L.; Claes, P.; Gruene, P.; Meijer, G.; Fielicke, A.; Nguyen, M. T.; Lievens, P. *ChemPhysChem* **2010**, *11*, 1932−1943.

(43) Churchill, M. R.; Hollander, F. J.; Hutchinson, J. P. *Inorg. Chem.* **1977**, *16*, 2655−2659.

(44) Mason, R.; Rae, A. *J. Chem. Soc. A* **1968**, 778−779.

(45) Slebodnick, C.; Zhao, J.; Angel, R.; Hanson, B. E.; Song, Y.; Liu, Z.; Hemley, R. J. *Inorg. Chem.* **2004**, *43*, 5245−5252.

(46) Delley, B.; Manning, M. C.; Ellis, D.; Berkowitz, J.; Trogler, W. C. *Inorg. Chem.* **1982**, *21*, 2247−2253.

(47) Braga, D.; Grepioni, F.; Tedesco, E.; Dyson, P. J.; Martin, C. M.; Johnson, B. F. *Transition Met. Chem.* **1995**, *20*, 615−624.